Physics Letters A 405 (2021) 127433

Contents lists available at ScienceDirect

Physics Letters A

www.elsevier.com/locate/pla

Investigation of deep levels in semi-insulating vanadium-doped 4H-SiC by photocurrent spectroscopy

Martin Rejhon, Mykola Brynza, Roman Grill, Eduard Belas, Jan Kunc *

Charles University, Faculty of Mathematics and Physics, Institute of Physics, Ke Karlovu 5, CZ-121 16, Prague 2, Czech Republic

ARTICLE INFO

Article history:
Received 8 February 2021
Received in revised form 23 April 2021
Accepted 16 May 2021
Available online 20 May 2021
Communicated by L. Ghivelder

Keywords:
Semi-insulating SiC
4H-SiC
Photocurrent spectroscopy
Deep levels
Localization radius

ABSTRACT

We measured spectral-resolved photocurrent in a wide range of photon energies from 0.68 eV to 4.10 eV, current-voltage characteristics, and mid to near-infrared transmittance spectra on a semi-insulating 4H-SiC wafer at room temperature. We identified four deep levels, their energies, and localization radii. The model considers the defects' wavefunction as a linear combination of s- and p-states. Such a linear combination leads to the mixture of dipole allowed and forbidden transitions. The forbidden transitions contribute to a broad photocurrent spectrum, and the allowed transitions appear as sharp photocurrent peaks. The width of photocurrent peaks is related to the localization radius of deep levels.

1. Introduction

High-purity semi-insulating silicon carbide (SiC) is a promising material for high-temperature, high-frequency, and high-power applications due to its bandgap energy [1,2], high saturation electron velocity, high breakdown field, and thermal conductivity [3]. SiC material has been investigated as a nuclear radiation detector in a hard radiation environment with excellent alpha particle detection properties [4–6]. However, the detection properties are mostly affected by the deep levels occurring in the material. Vanadium is a commonly used dopant of SiC to prepare semi-insulating crystals, which results in a low dark current. Vanadium is an amphoteric impurity in SiC lattice [7–9], existing in one of the three charge states. The charge state V^{5+} acts at a donor level, an acceptor level caused by V^{3+} charge state, and the last charge state is neutral V^{4+} [10]. The energy of these defect levels has been studied since 1990. However, the quality of the SiC material was poor with high density of imperfections [7–9,11–14].

The semi-insulating SiC was often studied under illumination due to the possible use as a photoconductive semiconductor switch [15,16]. The main method was the deep level transient spectroscopy (DLTS) [17] and current-mode DLTS (I-DLTS) [18–20]. These methods require a wide temperature range from cryogenic temperature to hundreds of kelvins to observe the semiconductor's energy levels.

In this paper, we present photocurrent spectroscopy measurements in a wide range of photon energy complemented with a theoretical approach as a simple method to observe optically active deep levels at room temperature. The photocurrent spectroscopy has been used to detect energy levels; nevertheless, the energy ranges were narrow [21–26]. Furthermore, to our best knowledge, no theoretical description was applied to the obtained photocurrent spectra. We combine photocurrent spectroscopy with an experimental and theoretical study of the I-V and transmittance spectrum measurements for a more complex analysis of deep levels. Besides their energies, we also determine localization radii of four vanadium-related point defects and contributions from the allowed and forbidden transitions. The allowed and forbidden transitions are a direct consequence of a mixed s- and p-states forming the deep levels.

2. Material and methods

The investigated samples were cut from the semi-insulating on-axis vanadium-doped 4H-SiC (II-IV inc.) substrate. The sample dimension is 5×5 mm^2, and the sample thickness is $L = 500$ µm. The Cr/Au electrical contacts were deposited on both opposite sides by evaporation. We use chromium as a reactive metal to improve the adhesion of the thicker gold layer. The samples were glued on the ceramic plate equipped with gold contacts by silver paste. The opposite metal contact was bonded to the second gold contact on the ceramic plate using silver wire and silver paste. Then, the sample was mounted in a cryostat to keep the temper-

* Corresponding author.
E-mail address: kunc@karlov.mff.cuni.cz (J. Kunc).

https://doi.org/10.1016/j.physleta.2021.127433
0375-9601/

Table 1
The table of wavelength ranges and corresponding photon flux value.

λ (nm)	1800-1150	1300-900	1000-750
Energy (eV)	0.69-1.08	0.95-1.38	1.24-1.65
Φ ($\times 10^{14}$ photons/cm^2 s)	13.50	6.03	2.54
λ (nm)	800-600	650-450	475-300
Energy (eV)	1.55-2.07	1.91-2.76	2.61-4.13
Φ ($\times 10^{14}$ photons/cm^2 s)	1.08	0.24	0.12

ature at 305 K in all measurements, using a thermoelectric cooler. The scheme of the apparatus is depicted in Fig. 1(a).

The I-V characteristic was measured in the range between −500 V and 500 V. A Keithley source 2410 was used to bias the sample, and a Keithley multimeter 2000 measured the voltage on a serial 1 GΩ resistor. The Schottky barrier heights were estimated from the I-V characteristic at higher applied voltages for both polarities. The photocurrent response to incident light was measured in the range of 0.68 eV and 4.10 eV to observe optically active deep levels in the sample. We illuminated the upper contact of the sample using monochromatic light from a monochromator (Fig. 1(a)), and the sample was biased at 500 V. The spectrum was measured separately for six different wavelength ranges. The photon flux was kept constant at each range using a neutral-density filter. The values of photon flux are listed in Table 1.

Two light-emitting diodes (LEDs) were used to measure a photocurrent dependency on the different photon fluxes. The first LED has a central wavelength at 630 nm with photon flux range between 2.3×10^{14} and 1.2×10^{16} photons/cm^2 s. The photon flux of the second LED with a central wavelength at 1200 nm varied between 1.1×10^{14} and 7.6×10^{15} photons/cm^2 s. The LED illuminated the top contact as monochromatic light during photocurrent measurement.

We also measured the sample's transmittance before the deposition of metal contacts to observe the correlations between the transmittance spectrum and the photocurrent spectrum. We used a Fourier Transform Infrared (FTIR) spectrometer Bruker Vertex80v in the spectral range between 0.5 eV and 2.5 eV. We used a nitrogen-cooled HgCdTe (uncooled Si) detector and KBr (CaF_2) beamsplitters for mid-(near-VIS)infrared measurements.

3. Results and discussion

The measured I-V characteristic without illumination depicted in Fig. 1(b) is symmetrical. It shows that there is no effect of the surface termination on the properties of the deposited metal contact because the contact properties are the same on both sides. The inset graph shows a linear dependence (in the logarithmic scale) of the current on the fourth root of the applied voltage V scale for higher voltages range < 40 V; 500 V$>$. It means that the sample contacts behave as an ideal Schottky barrier, and the current I can be described by the following equation [27]

$$I = AA^*T^2 \exp\left(-\frac{\phi_{B0}}{kT} + \frac{e}{kT}\sqrt{\frac{e}{4\pi\varepsilon}\sqrt{\frac{2eN_tV}{\varepsilon}}}\right). \quad (1)$$

Here, A is a contact area (25 mm^2), A^* is the Richardson constant for SiC (146 AK^{-2} cm^{-2}) [28], T is the absolute temperature (305 K), k is the Boltzmann constant, e is the elementary charge, $\varepsilon = \varepsilon_0\varepsilon_r$ is the permittivity of vacuum ε_0 and relative permittivity $\varepsilon_r = 10$, ϕ_{B0} is the Schottky barrier height, and N_t is the concentration of unbalanced trapped charge. The fit of the experimental data in the inset of Fig. 1(b) according to equation (1) leads to two fitting parameters. Schottky barrier height $\phi_{B0} = 1.2 - 1.4$ eV is similar for both polarities and the unbalanced trapped charge $N_t = 0.2 - 1.0 \times 10^{17}$ cm^{-3}. The observed value of doping is close to the expected value of vanadium doping ($N_t^{exp} \approx 1 \times 10^{17}$ cm^{-3}) based on the solubility of vanadium in SiC [29] and our Secondary Ion Mass Spectroscopy data (3×10^{17} cm^{-3}, spectra not shown here). The vanadium creates strong deep level around $E_c - 0.80$ eV, which pins the Fermi level close by [30–32]. Then the sample exhibits n-type conductivity [33]. We confirm the n-type doping by Hall effect and conductivity measurements. The Hall coefficient is $R_H = -8 \times 10^{11}$ cm^3 C^{-1} at 417 K (Fermi level $E_F = E_c - (0.80 - 0.85)$ eV, taking density-of-states effective mass $m^* = 0.77m_0$ and six-fold conduction band degeneracy including spin) and conductivity $\sigma = 1.5 \times 10^{-10}$ Ω^{-1} cm^{-1}. The corresponding electron mobility is $\mu = 120$ cm^2 V^{-1} s^{-1}. Fig. 1(c) shows the dependence of the photocurrent I_{ph} versus a central wavelength of illumination light. The photocurrent spectrum is measured in six different wavelength regions. All experimental points in the given spectral range are measured at the same photon flux, adjusted for each wavelength by a neutral density filter. The photon flux is presented in Table 1. However, to increase the dynamical range of our measurement, we change the photon flux between the spectral ranges. The measured photocurrent is proportional to the illumination power at a given wavelength, and it is proportional to the absorption of the sample. Our white light source was a halogen lamp with a maximal intensity at 1100-1200 nm, and the absorbance of our 0.5 mm thick vanadium doped SiC is on the order of 0.1 in NIR [34,35]. Hence, measuring with constant photon flux in the whole spectral range 300-1800 nm leads to increased noise in NIR (low illumination power, weak absorption). For this reason, we increased the signal-to-noise ratio by adjusting the photon flux for each spectral range from UV to NIR. We verified that the increased photon flux does not introduce any significant nonlinearity. Qualitatively, it is already evident from Fig. 1(c) that the overlapping parts have similar behavior. Quantitatively, we verified the linearity by light-emitting diodes (LED) at two wavelengths, 630 nm and 1200 nm, depicted in Fig. 1(c) by two vertical red dashed lines. Fig. 1(d) demonstrates this dependency in the log-log scale. The slope is 0.98 and 0.89 for LED 630 nm and LED 1200 nm, respectively. These values are close to 1, which means that we observe a linear behavior. The photocurrent linearity allows us to divide the measured spectra with the photon flux for each wavelength range.

Fig. 2 shows the normalized photocurrent I_{ph} spectrum (black points). The normalization was done by dividing each wavelength range by the incident photon flux Φ, presented in Table 1. The spectrum demonstrates the band-to-band excitation around the energy 3.30 eV which corresponds to the bandgap energy of 4H polytype ($E_G(300K) = 3.23$ eV [36]), shown by gray arrow in Fig. 2 (a). We also observe several photocurrent bands related to deep levels, shown by black arrows in Fig. 2 (a).

We attempted to describe the photocurrent spectra I_{ph} by a common Lucovsky model [37]

$$I_{Lucovsky} = \frac{I_0(\hbar\omega - E_i)^{3/2}}{(\hbar\omega)^3}, \quad (2)$$

given by the transition intensity I_0 and deep-level energy E_i. The Lucovsky model does not provide any variable parameter to adjust the high-energy tail of the photoconductivity peaks. We compare photocurrent spectra with the Lucovsky model in Fig. 2 (a). The Lucovsky model describes the photocurrent background signal well. However, it is not capable of describing the sharp spectral signals modulating the smooth background. The failure of Lucovsky model is well-known [38], and the model improvements include strong lattice-coupled defects. The lattice coupling is described by the Franck-Condon shift D and an effective phonon energy ε, and the absorption $I_{JP}(\hbar\omega, T)$ takes the integral form [39]

$$I_{JP}(\hbar\omega, T) = \frac{I_0}{\hbar\omega\sqrt{2\pi D\varepsilon \coth(\varepsilon/2k_BT)}}$$

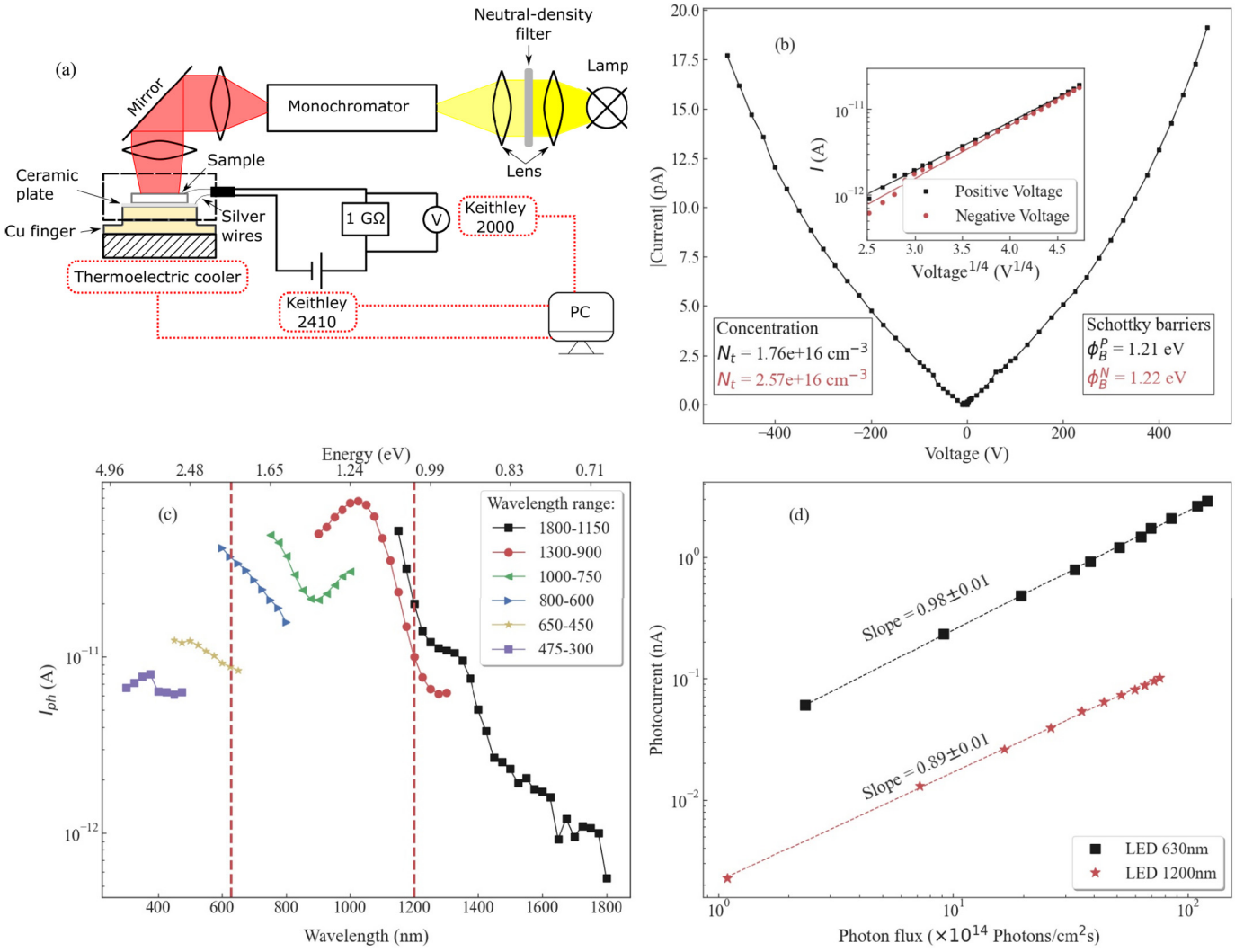

Fig. 1. (a) The scheme of the measured apparatus. (b) I-V characteristic at 305 K. Inset in Fig. 1(b) exhibits the relation between ln(I) and $U^{1/4}$.(c) Spectrum of measured photocurrent for each wavelength range. (d) The dependency of the photocurrent on the photon flux in log-log scale.

$$\times \int_0^\infty dE \frac{E^{3/2} \exp\left[-\frac{(\hbar\omega - E_0 - E)^2}{2D\epsilon \coth(\varepsilon/2k_B T)}\right]}{(E + E_0 - D)^2}, \qquad (3)$$

$$I_{Kireev} = \frac{I_0(\hbar\omega - E_i)}{(\hbar\omega)^2 \left(\hbar^2\chi^2/2m^* + \hbar\omega - E_i\right)^4}, \qquad (4)$$

where the energy $E_0 = E_i + D$. The model Eq. (3) is a convolution integral of the Lucovsky model Eq. (2) modified by the Franck-Condon shift D. Similar model was developed by Jaros [40]. Due to the convolution, the model Eq. (3) helps to explain the smooth onset of the absorption in the low-energy spectral range. However, it leads to the same high-energy scaling $(\hbar\omega)^{-3/2}$ as the Lucovsky model. The unchanged high-energy scaling was shown also in Ref. [41]. The reason of this slow high-energy tail is the neglected finite localization spread of the defect wavefunction in the evaluation of the transition matrix element in the Lucovsky work [37] and in the Jaros's work [40].

The defect wavefunction localization was taken into account in the work of Kireev [42], Joshi [43] and Inkson [44]. The results differ by the assumption on the defect wavefunction ψ_i. Inkson assumes $\psi_i \propto e^{-\chi r}/r$, where χ^{-1} is the defect localization radius ($\chi \to 0$ in the Lucovsky model). Kireev assumes $\psi_i \propto e^{-\chi r}$. Since the wavefunction should not be divergent, we take the Kireev's model. Here, I_{Kireev} characterizes the photo-ionization of the deep levels [42,43].

where $\hbar\omega$ is the energy of the incident photons, E_i is the deep level energy, $m^* = 0.77m_0$ is the effective mass of the density of states in the conduction band, m_0 is an electron mass, and χ^{-1} describes the localization radius of the defect. We note, that the exact shape of the wavefunction is always approximate, thus the localization radius is only an estimate of the actual wavefunction size.

The model Eq. (4) already describes the sharp photocurrent peaks well. However, it fails to describe the smooth background. This ambiguity can be resolved by looking at the symmetry of the defect wavefunction. The conduction band states consist mainly of the s-states, and the valence band states consist mainly of the p-states. The defect states should be more realistically described by the linear combination of the conduction band and valence band states [45]. The s- and p-contribution varies in the band gap similarly as in the case of the crystal termination by the surface, or, in the regime of the Schottky barrier formation [46]. Thus, the defect's wavefunction $|\psi_i\rangle = a|s\rangle + b|p\rangle$, a and b are linear coefficients, will lead to the combination of the dipole-allowed and dipole-forbidden transitions. The transitions from defect to the s-type conduction band are allowed from the defect's p-state, and

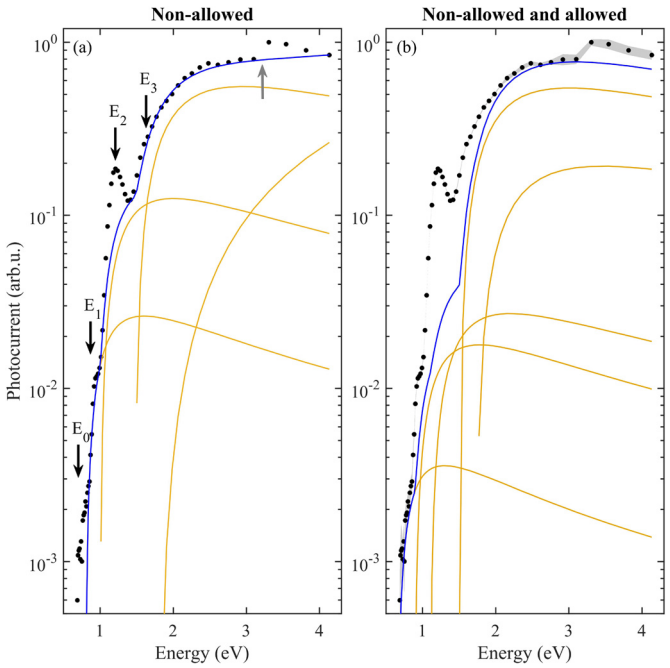

Fig. 2. (a) Photocurrent spectrum (black points) compared with the theoretical curve (blue curve) according to non-allowed transitions eq. (2), and (b) according to the combination of allowed and non-allowed transitions. The blue curve is again given by model (2). The fit is done self-consistently with the fit of allowed transitions, as shown in Fig. 3. Dark yellow curves also depict individual contributions from deep levels. The black arrows in (a) show the photocurrent sharp peaks above the smooth background signal caused by deep-level-conduction band transitions. The gray arrow depicts the interband transition between valence and conduction band. A gray band in (b) depicts an experimental error. (For interpretation of the colors in the figure(s), the reader is referred to the web version of this article.)

Table 2
Non-allowed transitions.

Level	E_i (eV)	I_0 (arb. u.)
E_0	$E_c - 0.65$	0.015
E_1	$E_c - 0.89$	0.12
E_2	$E_c - 1.1$	0.25
E_3	$E_c - 1.5$	8
E_4	$E_c - 1.73$	3.5

forbidden from the defect's s-state. Hence, the allowed transitions Eq. (4) should be present together with non-allowed (forbidden) transitions. Surprisingly, the non-allowed transitions are described by the same spectral dependence as the Lucovsky model Eq. (2), as shown by Inkson [44] and discussed by Passler [39], $I_{non-allowed} = I_{Lucovsky}$. The non-vertical allowed and non-allowed transitions can be distinguished by their spectral dependencies, too [44].

Motivated by the defect's mixed s- and p-states, we described the behavior of the measured photocurrent spectrum I_{ph} as a sum of the photocurrent $I_{allowed} = I_{Kireev}$ due to the allowed transitions and photocurrent $I_{non-allowed}$ due to the non-allowed transitions

$$I_{ph} = I_{allowed} + I_{non-allowed}. \quad (5)$$

Hence, we performed the data analysis in two steps. First, we determined the broad background caused by the non-allowed transitions, described by Eq. (2). The broad photocurrent background signals cause a large overlap of non-allowed transitions from many defects. The large overlap is prohibitive in determining all parameters for each transition reliably. We chose five non-allowed transitions, yellow curves in Fig. 2 (b), to effectively describe the smooth background. We summarize the fitting parameters in Table 2. The background fit was done under the constraint that the difference between the data and background has to be positive, shown in

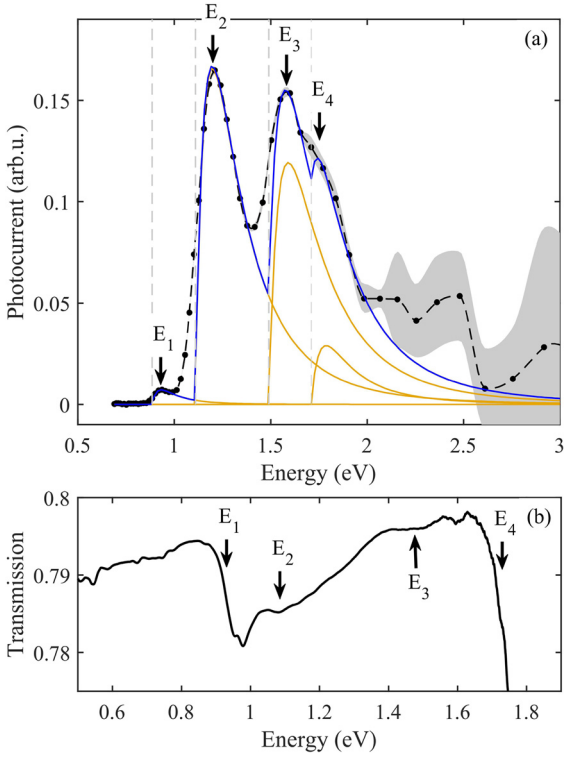

Fig. 3. (a) Photocurrent spectrum after subtraction of the smooth background signal shown in Fig. 2 (b). Experimental data (black points) are compared with theoretical curve (blue fit) according to allowed transitions Eq. (4). The individual photocurrent components are depicted by dark yellow curves. The dashed line is a guide for eye for experimental data and the gray area depicts an experimental error on 3σ confidence interval. (b) Optical transmission spectrum.

Fig. 2 (b), and we applied constraint on the energy position to fit the energies of deep-levels reported in literature [13,47,48]. We assume that the remaining positive spectrum is due to the allowed transitions. The allowed transitions are fitted by Eq. (4), and we compare the difference spectra with the model Eq. (4) in Fig. 3 (a). As the photocurrent spectrum should be proportional to the absorption, we also plot the transmission spectrum in Fig. 3 (b). The transmission spectrum is a combination of spectral flat Fresnel transmission and absorption. We depict the clear correspondence between the photopeaks and dips in the transmission (peaks in absorption) by arrows in Fig. 3 (b).

The background subtraction allows resolving up to three sharp photopeaks E_1, E_2. E_3 and we observe the fourth photopeak E_4 as a broader shoulder of E_3 transition. All four transitions are well-described only by the allowed defect-to-conduction band transitions, Eq. (4). All other models lead to too broad photopeaks without the possibility to adjust their widths. We summarize the fitted peak positions, intensities and widths (related to the localization radius) in Table 3 and graphically in Fig. 4.

We shall note that the high-energy photocurrent tails lead to a non-negligible contribution to photocurrent from several other deep levels. We point especially to the high energy tail of E_2 transition contributing to the photocurrent from E_3 and E_4. This overlap leads to reduced data fit reliability with increasing energy. The reliability can be improved by measuring in the wide spectral range and high dynamical range of detected photocurrent, as we presented in our methodology. Our data also show increased noise in the high photocurrent regime; see the gray area in Fig. 3 (a). Hence, we did not include these data in our analysis. The weak (strong) photocurrent signal below (above) ≈0.9 eV is a signature of the Fermi's level position. This is in agreement with our Hall effect and resistivity measurements $E_F = E_c - 0.78$ eV.

Table 3
Allowed transitions and their possible origins.

Level	E_i (eV)	I_0 (arb.u.)	χ^{-1} (Å)	Note
E_1	$E_c - 0.89$	2.4×10^{-4}	5.6	Vanadium acceptor level $V^{3+/4+}$ at h site, or oxygen related [7,13]
E_2	$E_c - 1.1$	7.5×10^{-2}	3.9	Vanadium complex [49,9,7], and/or carbon vacancy v_C^+ [8,33,13]
E_3	$E_c - 1.5$	1.4×10^{-1}	3.7	Vanadium donor level $V^{4+/5+}$ [8,7]
E_4	$E_c - 1.7$ ($E_v + 1.5$)	1.6×10^{-2}	4.4	Positively charged carbon vacancy v_C^+ [47,48]

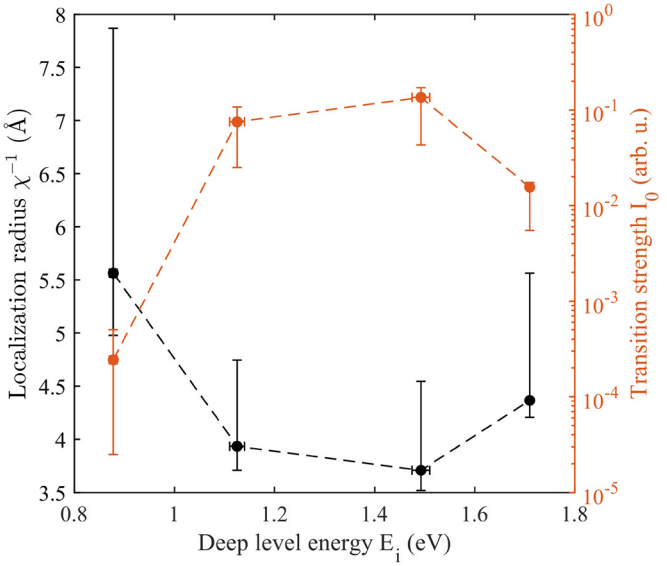

Fig. 4. (left) Deep-level localization radius plotted versus deep-level energy E_i from the bottom of conduction band E_c and (right) the transition strength I_0.

We also observe disagreement of the data with model (4) in the low-energy tails for transitions E_2, E_3 and E_4. These low-energy tails partially originate from the finite spectral resolution $\approx 20-25$ nm (70–90 meV) in VIS. This is the same order as the observed low-energy broadenning (≈100 meV). Another contribution to low-energy tails could be the Franck-Condon mechanism, as described by models of Jaros [40] or similar convolution integral of Passler [39], Eq. (3). Hence, we conclude that the change of the coordination coordinate is minimal. Such conclusion also explains why the photopeaks are energetically close to their binding energies E_i, apart from the model (3), where the photopeak maximum should be on the order of $2E_i$.

The localization radius plotted as a function of the deep-level energy in Fig. 4 suggests a possibly higher degree of wavefunction localization for levels deeper in the bandgap. Such scaling was discussed in literature [45], and it results from a simple quantum mechanical model. The shallow confinement potential provides only one bound state close to the continuum, and the wavefunction has long, exponentially-decaying tails. However, a deep confinement potential leads to the wavefunction with sharply attenuated tails and a higher degree of localization (an infinite potential well and hard-wall boundary conditions would be the limiting case for deep levels).

In the following we discuss a physical interpretation of the levels E_i, $i = \{0, 1, ..., 5\}$. The deep level $E_0 = E_c - 0.65$ eV could be connected with the vanadium acceptor level $V^{3+/4+}$ at quasi-cubic site ($E_c - 0.63$ eV), or with the $Z_{1/2}$ electron trap ($E_c - 0.68$ eV) [7,8,13]. We described this signal entirely by the non-allowed transition, hence, we could not determine the localization radius of this level reliably.

The deep level $E_1 = E_c - 0.89$ eV is interpreted as a vanadium acceptor level $V^{3+/4+}$ at h site [7,13]. The weak photocurrent leads to a higher experimental error of the localization parameter 5.6 Å. The overlap with the E_2 level photocurrent is another source of error to determine the localization parameter more precisely.

The strong photocurrent signal commences at level $E_2 = E_c - 1.1$ eV. The photopeak is well distinguished from other transitions in the vicinity of E_2, hence the localization radius 3.9 Å is determined with a smaller experimental error. The origin of level $E_2 = E_c - 1.1$ eV was unknown for long time [7]. Zvanut observed [8] the 1.1 eV level in both vanadium doped 4H-SiC and High Purity Semi-Insulating (HPSI) 4H-SiC without vanadium. This experimental work led to conclusion that the 1.1 eV level is related to carbon vacancies v_C^+ [8,33,13]. However, other works still pointed to the origin related to vanadium [7,9], or vanadium complex [49]. The electron paramagnetic resonance (EPR) showed that the 1.1 eV level does not represent a simply isolated impurity [9]. The localization radius of E_2 is 3.9 Å (3.7–4.7 Å) (4H-SiC lattice constant is 3.07 Å). The large radius and energy overlap leads us to suggest that the $E_2 = E_c - 1.1$ eV level is a vanadium-carbon vacancy complex. We also propose that the vanadium is in the interstitial position. The interstitial position follows from the electronegativity of vanadium, which replaces silicon in the SiC lattice. As the silicon sites are most likely occupied in the carbon vacancy's vicinity, vanadium might be, indeed, in the interstitial position. However, a density-functional theory (DFT) calculations will be necessary to confirm this proposed interpretation.

The level $E_3 = E_c - 1.5$ eV can be ascribed to the vanadium donor level $V^{4+/5+}$ [7,8]. The 3.7 Å small localization radius is in agreement with a simple quantum mechanical model of the mid-gap level.

The level $E_4 = E_c - 1.7$ eV is interpreted as a positively charged carbon vacancy v_C^+ [48]. The lower bound of the localization radius is above 4.2 Å, again, in agreement with closer proximity to the band edge.

Generally, our data analysis considering the defect's wavefunction as a mixture of s- and p-states is in agreement with early considerations of their composition [45]. The disagreement of Lucovsky model (2) was pointed in literature [39,38] and an improvement of the electronic part involved in the optical transitions was suggested by Passler [39]. Our analysis suggests that the Franck-Condon mechanism might be applicable for describing low-energy tails of photocurrent transitions. However, the defect's wavefunction localization radius determines the high-energy tails. The subtraction of the broad spectral background caused by non-allowed transitions is an essential step in data analysis. Other contributions to the smooth photocurrent background, not considered by us, could be the non-vertical transitions or, Schottky barrier at metal-semiconductor contacts. Although both contributions could be considered negligible, we did not draw any conclusions from the background data due to this ambiguity. We also note that the exact background determination influences the shape of sharp photocurrent peaks caused by allowed transitions negligibly. Hence, the separate analysis provides reliable energies and localization radii within the chosen defect's wave function model.

4. Conclusions

We investigated the influence of the deep levels in vanadium-doped 4H-SiC and the influence of the Schottky barrier height on the photocurrent spectrum in the energy range from 0.68 eV

to 4.1 eV. The Schottky barrier heights of metal contacts were determined from the I-V characteristics, which was symmetrical, pointing to negligible effect of the SiC face. The model consisting of deep level-to-conduction band and valence-to-conduction band transitions was successfully used to describe the observed photocurrent spectrum. We identified the role of allowed and non-allowed optical transitions on the photocurrent. Such a mixture of transitions is a direct consequence of the defect's wavefunction composed of the linear combination of s- and p-states. We explained the higher degree of localization of mid-gap states by a simple quantum-mechanical model. The evaluated deep defect energies were attributed to the vanadium point defect at quasi-cubic and h site, $Z_{1/2}$ electron trap, vanadium donor level, and positively charged carbon vacancy.

CRediT authorship contribution statement

Martin Rejhon: Experiment, Methodology, Formal Analysis, Writing - original draft. **Mykola Brynza**: Experiment. **Roman Grill**: Writing - review & editing. **Eduard Belas**: Funding acquisition, Writing - review & editing. **Jan Kunc**: Methodology, Sample fabrication, Formal Analysis, Writing - review & editing.

Declaration of competing interest

The authors declare that they have no known competing financial interests or personal relationships that could have appeared to influence the work reported in this paper.

Acknowledgements

This work was supported by the Czech Science Foundation project No. 18-12449S. CzechNanoLab project LM2018110 funded by MEYS CR is gratefully acknowledged for the financial support of the sample fabrication at CEITEC Nano Research Infrastructure.

References

[1] S. Doğan, A. Teke, D. Huang, H. Morkoç, C.B. Roberts, J. Parish, B. Ganguly, M. Smith, R.E. Myers, S.E. Saddow, 4H–SiC photoconductive switching devices for use in high-power applications, Appl. Phys. Lett. 82 (18) (2003) 3107–3109, https://doi.org/10.1063/1.1571667.

[2] K. Kelkar, N. Islam, C. Fessler, W. Nunnally, Silicon carbide photoconductive switch for high-power, linear-mode operations through sub-band-gap triggering, J. Appl. Phys. 98 (9) (2005) 093102, https://doi.org/10.1063/1.2126158.

[3] J.W. Palmour, C.H. Carter, C.E. Weitzel, K.J. Nordquist, High power and high frequency silicon carbide devices, MRS Proc. 339 (1994) 133, https://doi.org/10.1557/PROC-339-133.

[4] P.A. Bryant, A. Lohstroh, P.J. Sellin, Electrical characteristics and fast neutron response of semi-insulating bulk silicon carbide, IEEE Trans. Nucl. Sci. 60 (2) (2013) 1432–1435, https://doi.org/10.1109/tns.2013.2243753.

[5] A.R. Dulloo, F.H. Ruddy, J.G. Seidel, C. Davison, T. Flinchbaugh, T. Daubenspeck, Simultaneous measurement of neutron and gamma-ray radiation levels from a TRIGA reactor core using silicon carbide semiconductor detectors, IEEE Trans. Nucl. Sci. 46 (3) (1999) 275–279, https://doi.org/10.1109/23.775527.

[6] Y.B. Gurov, S.V. Rozov, V.G. Sandukovsky, E.A. Yakushev, L. Hrubcin, B. Zat'ko, Characteristics of silicon carbide detectors, Instrum. Exp. Tech. 58 (1) (2015) 22–24, https://doi.org/10.1134/s0020441215010054.

[7] W.C. Mitchel, W.D. Mitchell, G. Landis, H.E. Smith, W. Lee, M.E. Zvanut, Vanadium donor and acceptor levels in semi-insulating 4H- and 6H-SiC, J. Appl. Phys. 101 (1) (2007) 013707, https://doi.org/10.1063/1.2407263.

[8] M.E. Zvanut, V.V. Konovalov, H. Wang, W.C. Mitchel, W.D. Mitchell, G. Landis, Defect levels and types of point defects in high-purity and vanadium-doped semi-insulating 4H-SiC, J. Appl. Phys. 96 (10) (2004) 5484–5489, https://doi.org/10.1063/1.1797547.

[9] M.E. Zvanut, W. Lee, W.C. Mitchel, W.D. Mitchell, G. Landis, The acceptor level for vanadium in 4H and 6H SiC, Physica B, Condens. Matter 376–377 (1) (2006) 346–349, https://doi.org/10.1016/j.physb.2005.12.089.

[10] K. Maier, H.D. Müller, J. Schneider, Transition metals in silicon carbide (SiC): vanadium and titanium, Mater. Sci. Forum 83–87 (1992) 1183–1194, https://doi.org/10.4028/www.scientific.net/MSF.83-87.1183.

[11] J.R. Jenny, M. Skowronski, W.C. Mitchel, H.M. Hobgood, R.C. Glass, G. Augustine, R.H. Hopkins, On the compensation mechanism in high-resistivity 6H–SiC doped with vanadium, J. Appl. Phys. 78 (6) (1995) 3839–3842, https://doi.org/10.1063/1.359899.

[12] N. Achtziger, W. Witthuhn, Band gap states of Ti, V, and Cr in 4H–silicon carbide, Appl. Phys. Lett. 71 (1) (1997) 110–112, https://doi.org/10.1063/1.119485.

[13] P. Kamiński, R. Kozłowski, M. Miczuga, M. Pawłowski, M. Kozubal, M. Pawłowski, High-resolution photoinduced transient spectroscopy of defect centers in vanadium-doped semi-insulating SiC, J. Mater. Sci., Mater. Electron. 19 (S1) (2008) 224–228, https://doi.org/10.1007/s10854-008-9576-6.

[14] R.R. Ciechonski, M. Syväjärvi, A. Kakanakova-Georgieva, R. Yakimova, Effect of boron on the resistivity of compensated 4H-SiC, J. Electron. Mater. 32 (5) (2003) 452–457, https://doi.org/10.1007/s11664-003-0177-0.

[15] S. Jiang, C. Song, L. Zhang, Y. Zhang, W. Huang, H. Guo, Intrinsic photoconductive switches based on semi-insulator 4H-SiC, IEEE Trans. Electron Devices 63 (4) (2016) 1582–1586, https://doi.org/10.1109/ted.2016.2526642.

[16] J.S. Sullivan, J.R. Stanley, 6H-SiC photoconductive switches triggered at below bandgap wavelengths, IEEE Trans. Dielectr. Electr. Insul. 14 (4) (2007) 980–985, https://doi.org/10.1109/tdei.2007.4286537.

[17] K. Murata, T. Tawara, A. Yang, R. Takanashi, T. Miyazawa, H. Tsuchida, Wide-ranging control of carrier lifetimes in n-type 4H-SiC epilayer by intentional vanadium doping, J. Appl. Phys. 126 (4) (Jul 2019), https://doi.org/10.1063/1.5098101.

[18] G. Alfieri, T. Kimoto, G. Pensl, Deep levels observed in high-purity semi-insulating 4H-SiC, Mater. Sci. Forum 645–648 (2010) 455–458, https://doi.org/10.4028/www.scientific.net/MSF.645-648.455.

[19] G. Alfieri, L. Knoll, L. Kranz, V. Sundaramoorthy, The effects of illumination on deep levels observed in as-grown and low-energy electron irradiated high-purity semi-insulating 4H-SiC, J. Appl. Phys. 123 (17) (2018) 175304, https://doi.org/10.1063/1.5023337.

[20] M. Kato, K. Kito, M. Ichimura, Deep levels affecting the resistivity in semi-insulating 6H-SiC, J. Appl. Phys. 108 (5) (2010) 053718, https://doi.org/10.1063/1.3481095.

[21] S.A. Reshanov, V.P. Rastegaev, Photoconductivity of semi-insulating SiC:V, Al, Diam. Relat. Mater. 10 (11) (2001) 2035–2038, https://doi.org/10.1016/s0925-9635(01)00475-7.

[22] J. Choi, J. Chang, Photoconductivity of AlN films on SiC, J. Appl. Phys. 98 (9) (2005) 093513, https://doi.org/10.1063/1.2126787.

[23] L. Conte, U. Coscia, D.K. Basa, G. Ambrosone, V. Rigato, Spectral photoconductivity of nanostructured silicon carbon films spectral photoconductivity of SiC thin films, in: 2014 Fotonica AEIT Italian Conference on Photonics Technologies, 2014, pp. 1–4.

[24] E.V. Kalinina, G.N. Violina, I.P. Nikitina, E.V. Ivanova, V.V. Zabrodski, M.Z. Shvarts, S.A. Levina, A.V. Nikolaev, Effect of temperature on the characteristics of 4H-SiC UV photodetectors, Semiconductors 54 (2) (2020) 246–252, https://doi.org/10.1134/s1063782620020128.

[25] M. Kato, K. Miyake, T. Yasuda, M. Ichimura, T. Hatayama, T. Ohshima, Spectral response, carrier lifetime, and photocurrents of SiC photocathodes, Jpn. J. Appl. Phys. 55 (1, SI) (2016) 01AC02, https://doi.org/10.7567/JJAP.55.01AC02.

[26] M. Kato, N. Ichikawa, Y. Nakano, Characterisation of defects in p-type 4H-, 6H- and 3C-SiC epilayers grown on SiC substrates, Mater. Lett. 254 (2019) 96–98, https://doi.org/10.1016/j.matlet.2019.07.043.

[27] S.M. Sze, K.K. Ng, Physics of Semiconductor Devices, 3rd edition, Wiley-Interscience, Hoboken, N.J., 2006.

[28] A. Itoh, T. Kimoto, H. Matsunami, High performance of high-voltage 4H-SiC Schottky barrier diodes, IEEE Electron Device Lett. 16 (6) (1995) 280–282, https://doi.org/10.1109/55.790735.

[29] J.R. Jenny, J. Skowronski, W.C. Mitchel, H.M. Hobgood, R.C. Glass, G. Augustine, R.H. Hopkins, Deep level transient spectroscopic and Hall effect investigation of the position of the vanadium acceptor level in 4H and 6H SiC, Appl. Phys. Lett. 68 (14) (1996) 1963–1965, https://doi.org/10.1063/1.115640.

[30] T. Dalibor, G. Pensl, H. Matsunami, T. Kimoto, W.J. Choyke, A. Schöner, N. Nordell, Deep defect centers in silicon carbide monitored with deep level transient spectroscopy, Phys. Status Solidi A 162 (1) (1997) 199–225, https://doi.org/10.1002/1521-396x(199707)162:1<199::Aid-pssa199>3.0.Co;2-0.

[31] V. Lauer, G. Brémond, A. Souifi, G. Guillot, K. Chourou, M. Anikin, R. Madar, B. Clerjaud, C. Naud, Electrical and optical characterisation of vanadium in 4H and 6H–SiC, Mater. Sci. Eng. B 61–62 (1999) 248–252, https://doi.org/10.1016/s0921-5107(98)00512-1.

[32] V. Lauer, G. Brémond, A. Souifi, G. Guillot, K. Chourou, R. Madar, B. Clerjaud, Spectroscopic investigation of vanadium acceptor level in 4H and 6H-SiC, Mater. Sci. Forum 338–342 (2000) 635–638, https://doi.org/10.4028/www.scientific.net/MSF.338-342.635.

[33] W. Mitchel, W. Mitchell, M. Zvanut, G. Landis, High temperature Hall effect measurements of semi-insulating 4H-SiC substrates, in: International Semiconductor Device Research Symposium (ISDRS 03), Washington, DC, DEC 10-12, 2003, Solid-State Electron. 48 (10–11) (2004) 1693–1697, https://doi.org/10.1016/j.sse.2004.02.025.

[34] M. Bickermann, R. Weingartner, A. Winnacker, On the preparation of vanadium doped PVT grown SiC boules with high semi-insulating yield, J. Cryst. Growth 254 (3–4) (2003) 390–399, https://doi.org/10.1016/S0022-0248(03)01179-5.

[35] N.J. Kramer, L.F. Voss, A.M. Conway, P.V. Grivickas, M. Bora, D.L. Hall, A.N. Caruso, Extrinsic absorption pathways in vanadium-doped sic measured using a total internal reflection geometry, Phys. Status Solidi A, Appl. Mater. Sci. 217 (20) (Oct 2020), https://doi.org/10.1002/pssa.202000315.
[36] M.E. Levinshtein, S.L. Rumyantsev, M. Shur, Properties of Advanced Semiconductor Materials, Wiley, New York, 2001.
[37] G. Lucovsky, On the photoionization of deep impurity centers in semiconductors, Solid State Commun. 3 (9) (1965) 299–302, https://doi.org/10.1016/0038-1098(65)90039-6.
[38] P. Klein, S. Binari, J. Freitas, A. Wickenden, Photoionization spectroscopy of traps in GaN metal-semiconductor field-effect transistors, J. Appl. Phys. 88 (5) (2000) 2843–2852, https://doi.org/10.1063/1.1287127.
[39] R. Passler, Photoionization cross-section analysis for a deep trap contributing to current collapse in GaN field-effect transistors, J. Appl. Phys. 96 (1) (2004) 715–722, https://doi.org/10.1063/1.1753076.
[40] M. Jaros, Wave-functions and optical cross-sections associated with deep centers in semiconductors, Phys. Rev. B 16 (8) (1977) 3694–3706, https://doi.org/10.1103/PhysRevB.16.3694.
[41] A. Alkauskas, M.D. McCluskey, C.G. Van de Walle, Tutorial: defects in semiconductors-combining experiment and theory, J. Appl. Phys. 119 (18) (May 2016), https://doi.org/10.1063/1.4948245.
[42] P.J. Kireev, Semiconductor Physics, Mir Publishers, Moscow, 1978.
[43] N.V. Joshi, B. Vincent, Study of photoionization cross section of shallow donors in CdTe, Phys. Lett. A 92 (9) (1982) 476–478, https://doi.org/10.1016/0375-9601(82)90388-7.
[44] J. Inkson, Deep impurities in semiconductors. 2. The optical-cross-section, J. Phys. C, Solid State Phys. 14 (7) (1981) 1093–1101, https://doi.org/10.1088/0022-3719/14/7/012.
[45] D. Lang, R. Logan, M. Jaros, Trapping characteristics and a donor-complex (DX) model for the persistent photoconductivity trapping center in Te-doped $Al_xGa_{1-x}As$, Phys. Rev. B 19 (2) (1979) 1015–1030, https://doi.org/10.1103/PhysRevB.19.1015.
[46] R.T. Tung, The physics and chemistry of the Schottky barrier height, Appl. Phys. Rev. 1 (1) (Mar 2014), https://doi.org/10.1063/1.4858400.
[47] A. Lebedev, Deep level centers in silicon carbide: a review, Semiconductors 33 (2) (1999) 107–130, https://doi.org/10.1134/1.1187657.
[48] E. Janzen, I. Ivanov, N. Son, B. Magnusson, Z. Zolnai, A. Henry, J. Bergman, L. Storasta, F. Carlsson, Defects in SiC, in: 22nd International Conference on Defects in Semiconductors (ICDS-22), UNIV Aarhus, Aarhus, Denmark, Jul 28-Aug 01, 2003, Phys. Rev. B, Condens. Matter 340 (2003) 15–24, https://doi.org/10.1016/j.physb.2003.09.001.
[49] A. Evwaraye, S. Smith, W. Mitchel, Shallow and deep levels in n-type 4H-SiC, J. Appl. Phys. 79 (10) (1996) 7726–7730, https://doi.org/10.1063/1.362376.